

To be published in Optics Letters:

Title: Resolving multi-path interference in time-of-flight imaging via modulation frequency diversity and sparse regularization

Authors: Christopher Barsi, Ramesh Raskar, Achuta Kadambi, Ayush Bhandari, Micha Feigin-Almon, Adrian Dorrington, and Refael Whyte

Accepted: 7 February 2014

Posted: 10 February 2014

Doc. ID: 201075

Published by

OSA

Resolving multi-path interference in time-of-flight imaging via modulation frequency diversity and sparse regularization

Ayush Bhandari¹, Achuta Kadambi¹, Refael Whyte^{1,2}, Christopher Barsi^{1,*}, Micha Feigin¹, Adrian Dorrington², and Ramesh Raskar¹

¹MIT Media Lab, Massachusetts Institute of Technology, 77 Massachusetts Ave, Cambridge, MA 02139

²School of Engineering, University of Waikato, Private Bag 3105, Hamilton, 3240, New Zealand

*Corresponding author: cbarisi@mit.edu

Compiled February 5, 2014

Time-of-flight (ToF) cameras calculate depth maps by reconstructing phase shifts of amplitude-modulated signals. For broad illumination or transparent objects, reflections from multiple scene points can illuminate a given pixel, giving rise to an erroneous depth map. We report here a sparsity-regularized solution that separates K interfering components using multiple modulation frequency measurements. The method maps ToF imaging to the general framework of spectral estimation theory and has applications in improving depth profiles and exploiting multiple scattering. © 2014 Optical Society of America

OCIS codes: 110.6880, 100.6890, 150.5670, 120.0280

Time-of-flight (ToF) sensing offers solutions for several optical ranging and surface profiling applications, such as image-guided surgery [1], gesture recognition [2], remote sensing [3], and shape [4] and phase [5] measurements. Although ToF sensors can be impulse-based, commercial versions often rely on the continuous wave approach [6]: the source intensity is modulated at radio frequencies (~ 10 s of MHz), and the detector reconstructs the phase shift between the reflected and emitted signals. Distance is calculated by scaling the phase by the modulation frequency (Fig. 1(a)). This method, amplitude modulated continuous wave (AMCW) ToF, offers suitable SNR for real-time, consumer applications [7–9].

However, AMCW ToF suffers from multi-path interference (MPI) [10–17]. Consider the scenes in Figs. 1(b,c). Light rays from multiple reflectors scatter to the observation point. Each path acquires a different phase shift, and the measurement consists of the sum of these components. The recovered phase, therefore, is incorrect. Such “mixed” pixels contain depth errors and arise in global lighting conditions, when an observation point is illuminated indirectly by, e.g., inter-reflections, translucent sheets, and subsurface scattering [18]. In some cases (Fig. 1(d)), MPI comprises a continuum of scattering paths. Previous suggested solutions include structured light or mechanical scanning [19, 20], but these are limited by the source resolution. Computational optimization schemes [21, 22] rely on radiometric assumptions and have limited applicability.

Here, we resolve MPI via sparse regularization of multiple modulation frequency measurements. The formulation allows us to recast this problem into the general framework of spectral estimation theory [23]. This contribution generalizes the dual-frequency approach [13–15] to account for more than two components. Thus, our method here has two significant benefits. First, we sepa-

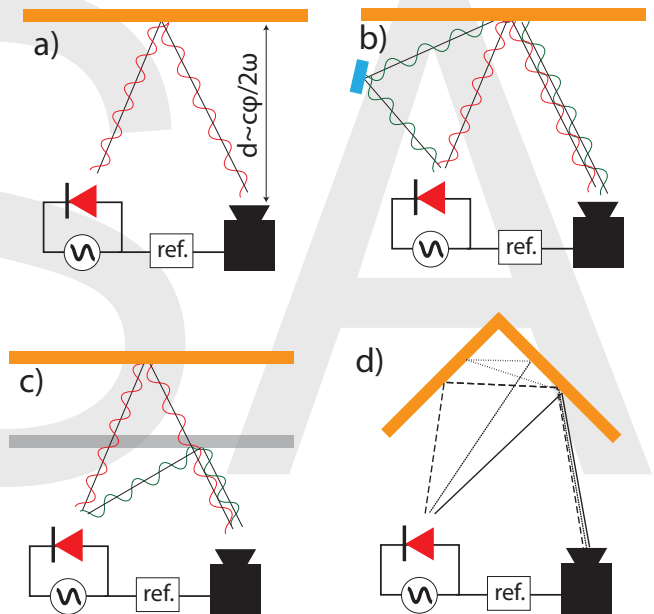


Fig. 1. (a) ToF principle: the phase delay of an emitted AMCW wave proportionally encodes the distance of the object. (b) Mirror-like and (c) semi-transparent reflections produce MPI and yield an incorrect phase. (c) A complicated scene with continuous MPI.

rate MPI from direct illumination to produce improved depth maps. Second, we resolve MPI into its components, so that we can characterize and exploit multiple scattering phenomena. The procedure has two steps: (1) record a scene with multiple modulation frequencies and (2) reconstruct the MPI components using a sparsity constraint. We also discuss the possible extension to continuous scattering (e.g., Fig. 1(d)).

Consider first the single-component case. Mathemati-

cally, the camera emits the normalized time-modulated intensity $s(t)$ ¹ and detects a signal $r(t)$:

$$s(t) = 1 + s_0 \cos(\omega t), t \in \mathbb{R} \quad (1a)$$

$$r(t) = \Gamma(1 + s_0 \cos(\omega t - \phi)). \quad (1b)$$

Here, s_0 and $\Gamma \in [0, 1]$ are the signal modulation amplitude and the reflection amplitude, respectively, ω is the modulation frequency, and ϕ is the phase delay between the reference waveform $s(t)$ and the delayed version $r(t)$. For a co-located source and detector, the distance to the object from the camera is given by the relation $d = c\phi/2\omega$, where c is the speed of light.

Electronically, each pixel acts as a homodyne detector and measures the cross-correlation between the reflected signal and the reference [6]. Denoting the complex conjugate of $f \in \mathbb{C}$ by f^* , the cross-correlation of two functions f and g is

$$C_{f,g}(\tau) \stackrel{\text{def}}{=} \lim_{T \rightarrow \infty} \frac{1}{2T} \int_{-T}^{+T} f^*(t + \tau) g(t) dt. \quad (2)$$

Note that infinite limits are approximately valid when the integration window $2T$ is such that $T \gg \omega^{-1}$. A shorter time window produces residual errors, but this is avoidable in practice. The pixel samples the cross-correlation at discrete times τ_q :

$$m_\omega[q] \stackrel{\text{def}}{=} C_{s,r}(\tau_q) \stackrel{(2)}{=} \Gamma \left(1 + \frac{s_0^2}{2} \cos(\omega\tau_q + \phi) \right). \quad (3)$$

Using 4-Bucket Sampling [7], we calculate the estimated reflection amplitude and phase, $\tilde{\Gamma}, \tilde{\phi}$, with four samples $\tau_q = \pi q/2\omega$ with $q = 0, \dots, 3$:

$$\tilde{\Gamma} = \sqrt{(m_\omega[3] - m_\omega[1])^2 + (m_\omega[0] - m_\omega[2])^2} / s_0^2, \quad (4a)$$

$$\tan \tilde{\phi} = \left(\frac{m_\omega[3] - m_\omega[1]}{m_\omega[0] - m_\omega[2]} \right). \quad (4b)$$

Therefore, we associate a complex value, z_ω , with a pixel measurement:

$$z_\omega = \tilde{\Gamma} e^{j\tilde{\phi}(\omega)}. \quad (5)$$

Note that these results are formally equivalent to phase reconstruction via phase-shifting digital holography [24].

When multiple reflections contribute to a single measurement, the return signal comprises a sum. In phasor notation, for K components,

$$r(t) = C_0 + \sum_{k=0}^{K-1} \Gamma_k e^{j(\omega t - \phi_k(\omega))}, \quad (6)$$

where C_0 is a constant, $\phi_k(\omega) = 2d_k\omega/c$, and $\{d_k\}_{k=0}^{K-1}$ are K depths at which the corresponding reflection takes place. The reflection amplitude of the k^{th} surface is Γ_k . Each pixel records

$$m_\omega^K[q] = C_0 + \frac{s_0^2}{2} e^{j\omega\tau_q} \sum_{k=0}^{K-1} \Gamma_k e^{j\phi_k(\omega)}. \quad (7)$$

¹Here, we consider sinusoidal imaging, but the discussion is applicable to any periodic function.

Importantly, for a given modulation frequency ω_0 (ignoring a constant DC term), $m_{\omega_0}^K[\tau_q] \propto \exp(j\omega_0\tau_q)$, i.e., there is no variation with respect to individual depth components $\{\Gamma_k, \phi_k\}_{k=0}^{K-1}$ [16], regardless of the sampling density. Equivalently, the camera measurement,

$$z_\omega^{(K)} = \tilde{\Gamma}(\omega) e^{j\tilde{\phi}(\omega)} = \sum_{k=0}^{K-1} \Gamma_k e^{j\phi_k(\omega)} \quad (8)$$

is now a complex sum of K reflections, which cannot be separated without independent measurements. Thus, at a given frequency, the measured phase, and hence the depth, is a nonlinear mixture of all interfering components.

Our method separates these components by recording the scene with equi-spaced frequencies $\omega = n\omega_0$ ($n \in \mathbb{N}$) and acquiring a set of measurements \mathbf{z} :

$$\mathbf{z} = \left(z_{\omega_0}^{(K)}, z_{2\omega_0}^{(K)}, \dots, z_{N\omega_0}^{(K)} \right)^\top. \quad (9)$$

The forward model can be written compactly in vector-matrix form as $\mathbf{z} = \mathbf{\Phi}\mathbf{g} + \boldsymbol{\sigma}$, where $\mathbf{\Phi} \in \mathbb{C}^{N \times K}$ is identified as a Vandermonde matrix,

$$\mathbf{\Phi} = \begin{pmatrix} e^{j\omega_0\phi_0} & e^{j\omega_0\phi_1} & \dots & e^{j\omega_0\phi_{K-1}} \\ e^{j2\omega_0\phi_0} & e^{j2\omega_0\phi_1} & \dots & e^{j2\omega_0\phi_{K-1}} \\ \vdots & \vdots & \ddots & \vdots \\ e^{jN\omega_0\phi_0} & e^{jN\omega_0\phi_1} & \dots & e^{jN\omega_0\phi_{K-1}} \end{pmatrix}, \quad (10)$$

$\mathbf{g} = [\Gamma_0, \dots, \Gamma_{K-1}]^\top \in \mathbb{R}^{K \times 1}$, and $\boldsymbol{\sigma}$ represents zero-mean Gaussian i.i.d. noise, which controls the error ε_0 in our reconstruction algorithm. Our goal is to estimate the phases $\boldsymbol{\phi} = [\phi_0, \dots, \phi_{K-1}]^\top \in \mathbb{R}^{K \times 1}$ and the reflection amplitude vector \mathbf{g} .

To recover these quantities, first note the similarity between $\mathbf{\Phi}$ and an oversampled $N \times L$ discrete Fourier transform (DFT) matrix $\boldsymbol{\Psi}$, with elements $\Psi_{nl} = \exp(jnl/L)$. If $L \gg K$, the discretization of $\boldsymbol{\Psi}$ is small enough to assume that the columns of $\mathbf{\Phi}$ are contained in $\boldsymbol{\Psi}$. We can also define a vector $\mathbf{g}' \in \mathbb{R}^{L \times 1}$, whose elements are zero except for K reflection amplitudes $\{\Gamma_k\}_{k=0}^{K-1}$, such that $\mathbf{z} = \boldsymbol{\Psi}\mathbf{g}'$. We use the (K) -sparsity of \mathbf{g}' to regularize the problem:

$$\underbrace{\|\mathbf{z} - \boldsymbol{\Psi}\mathbf{g}'\|_{\ell_2}^2}_{\text{Data-Fidelity}} < \varepsilon_0 \quad \text{such that} \quad \underbrace{\|\mathbf{g}'\|_{\ell_0}}_{\text{Sparsity}} = K, \quad (11)$$

where the ℓ_p -norm is $\|\mathbf{x}\|_{\ell_p}^p \stackrel{\text{def}}{=} \sum_n |x_n|^p$. The limit $p \rightarrow 0$ is used to define $\|\mathbf{g}'\|_{\ell_0}$ as the number of nonzero elements of \mathbf{g}' . Eq. 11 demands a least-squares solution to the data-fidelity problem $\|\mathbf{z} - \boldsymbol{\Psi}\mathbf{g}'\|_{\ell_2}^2$ up to some error tolerance ε_0 , with the constraint that we accommodate up to K nonzero entries of \mathbf{g}' . For three components ($K = 3$), we choose $\boldsymbol{\Psi}$ to have $L = 62832$ columns. Therefore, the resulting discretization error is $\pm 2\pi/2L = \pm 0.05$ mrad (though the total error includes contributions from other sources, such as sensor noise).

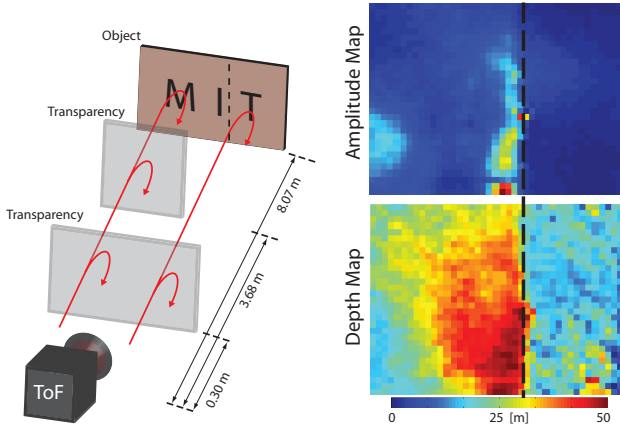


Fig. 2. Left: experimental setup. Two transparencies block the left side of the camera (three components), and one transparency blocks the right (two components). Right: measured amplitude and depth at $\omega = 3\omega_0$. Dashed line indicates edge of second transparency.

The sparsity of \mathbf{g}' arises from two assumptions. First, we ignore the inter-reflections between scattering layers, as their amplitudes fall off quickly. Second, we do not consider volumetric scattering, which precludes discrete reflections and requires a different parameterization (e.g., diffusion coefficients). However, even in the continuum case (e.g., Fig. 1d), there is potential for relative improvement using our method: we can approximate the continuum by a finite number of reflections, with the discretization set by the system resolution and the total number limited by the falloff in amplitude. This approximate model then can be applied here.

We solve Eq. 11 via orthogonal matching pursuit (OMP) [25], which iteratively searches for the best-fit projections (in the least-squares sense) of the coefficients onto an over-complete dictionary. We input Ψ and measurements \mathbf{z} into the algorithm. The outputs are the set of reflection coefficients Γ_k and their positions, l_k , in \mathbf{g}' . With the position of each Γ_k recovered, the corresponding phases ϕ_k are recovered through the elements of each non-zero Ψ : $\phi_k = (jn)^{-1} \log(\Psi_{nl_k}) = l_k/L$.

We verify this theory with the experimental setup shown in Fig. 2. A PMD19k-2 160×120 sensor array is controlled by a Stratix III FPGA. Analog pixel values are converted to 16-bit unsigned values by an ADC during the pixel readout process. Eight 100 mW Sony SLD 1239JL-54 laser diodes illuminate the scene. The lasers are placed symmetrically around the detector for a coaxial configuration. The base frequency modulation is $f_0 = \omega_0/2\pi = 0.7937$ MHz, and the integration time is 47 ms. The scene consists of three layers. Farthest, at 8.1 m, is an opaque wall with gray-scale text (“MIT”) printed on it. Closest, at 0.3 m, is a semi-transparent sheet. Between the two layers is another semi-transparent sheet that covers only the left half of the field of view. Therefore, the left-hand side records

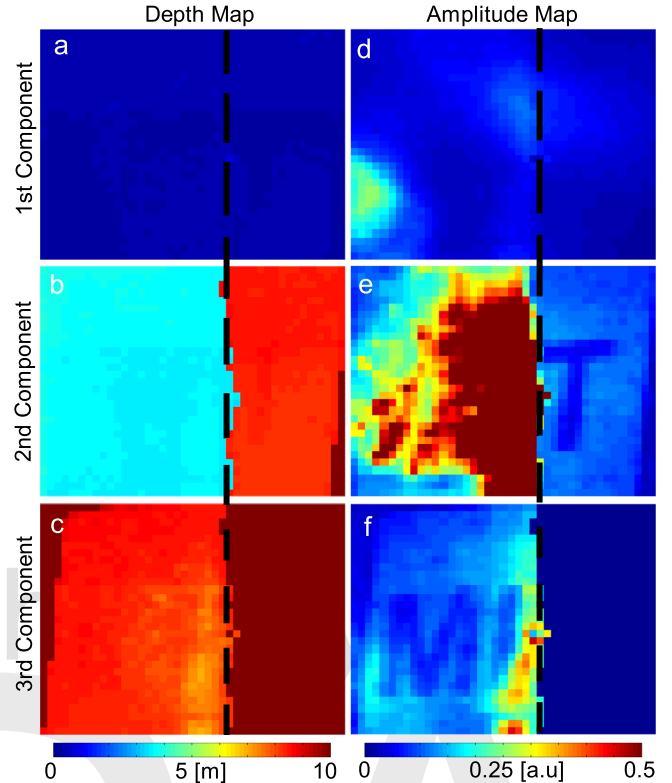


Fig. 3. Reconstructed amplitudes and depths via sparse regularization. Dashed lines indicate edge of second transparency.

three bounces and the right only two. All layers are within the camera’s depth of field to avoid mixed pixels from blurring.

Depth and amplitude maps acquired at a specific frequency are shown in Fig. 2. Due to MPI, the measured depths do not correspond to any physical layer in the scene. All depth and amplitude information from the three scene layers is mixed nonlinearly into a set of composite measurements (pixels) and cannot be recovered.

A total of 77 modulation frequencies, spaced 0.7937 MHz apart, are acquired and input into the OMP algorithm with $K = 3$. The reconstruction, shown in Fig. 3, shows each depth correctly recovered. The closest depth map (Fig. 3(a), first transparency) is constant. The second map (Fig. 3(b)) contains two depths: the second transparency on the LHS and the wall on the RHS. The third depth map contains the wall depth on the LHS (Fig. 3(c)). The third-bounce amplitude (Fig. 3(f)) is zero where there are only two layers (RHS). The depth here is therefore undefined, though we set the distance to be 10 m for visual clarity. Further, the text is recovered properly in the amplitude maps corresponding to the correct depths (Figs. 3(e,f)). Note that accurate depths are recovered even in the presence of strong specularities (Fig. 3(e)).

Fig. 4 shows a histogram of reconstructed distances. Distances in the mixed-pixel measurement (Fig. 2) vary

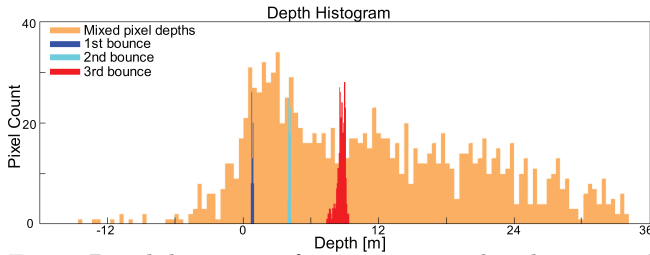


Fig. 4. Depth histogram for reconstructed and measured depth maps. Reconstructed distances cluster around the correct depths, whereas the MPI depth map has a wide variance across the entire range.

continuously across a 30 m range. (A fixed 18.56 m global offset, due to differences in cable lengths and electronic timing, yields negative depths in mixed pixel histogram.) The reconstructed distances are 0.19 m, 3.6 m, and 8.1 m, which agree with the ground truth values in Fig. 2 to within the experimental accuracy. The relative differences are within 3% of the true values. The third-phase variance is wider because OMP computes the first two components, leaving little residual energy, so that several columns in Ψ can minimize the least-squares error.

In principle, the technique can be extended to any number of bounces, provided enough modulation frequencies are used (though a first-principles derivation is beyond the scope of this contribution). In practice, however, the reflected amplitudes decrease with increasing component number, so that higher-order components diminish in importance. Furthermore, OMP need not assume a number of components that is the same as that of the physical implementation. If the assumed number is greater than the physical number, OMP will reconstruct all the physical components, with higher-order ones having an amplitude on order of the system noise. Conversely, if the assumed number is less than the physical number, OMP will recover the strongest reflections.

Therefore, the method is a generalization of global/direct illumination separation and can decompose different elements of global lighting. This is useful not only for improved depth accuracy, but also imaging in the presence of multiple scatterers such as diffuse layers, sediment, turbulence, and turbid media, as well as in places where third-component scattering must be extracted [26]. Furthermore, because it is based on phase measurements, this technique can be mapped to multiple scattering in holography [27] by substituting optical frequency for the modulation frequency.

In conclusion, we implemented a multi-frequency approach for decomposing multiple depths for a ToF camera. The result is general and holds for any number of bounces, and it can be extended to non-harmonic signals [17]. Future work includes calculating bounds on measurements and resolution. The method can be incorporated with structured illumination and pixel correlations for edge detection and refocusing. The result holds promise for mitigating and exploiting MPI for a wide variety of scenes.

This work was supported by NSF grant 1115680, Charles Stark Draper grant SC001-744, and ISN grant 6927356. R.W. was supported by a University of Waikato Doctoral Scholarship.

References

1. D. M. Cash, T. K. Sinha, W. C. Chapman, H. Terawaki, B. M. Dawant, R. L. Galloway, and M. I. Miga, *Med. Phys.* **30**, 1671–1682 (2003).
2. P. Breuer, C. Eckes, and S. Müller, 247–260 (Springer, 2007).
3. M. C. Amann, T. Boch, R. Myllylä, M. Rioux, and M. Lescure, *Opt. Eng.* **40**, 10–19 (2001).
4. Y. Cui, S. Schoun, D. Chan, S. Thrun, and C. Theobalt, *Proc. CVPR IEEE*, 1173–1180 (2010).
5. J. C. Halimeh and M. Wegener, *Opt. Express* **20**, 63–74 (2012).
6. R. Lange, and P. Seitz, *IEEE J. Quant. Elect.* **37**, 390–397 (2001).
7. S. Foix, G. Alenya, and C. Torras, *IEEE Sens. J.* **11**, 1917–1926 (2011).
8. A. Kolb, E. Barth, R. Koch, and R. Larsen, *Proc. Eurographics*, 119–134 (2009).
9. M. Hansard, S. Lee, O. Choi, and R. Horaud (Springer, 2013).
10. M. Frank, M. Plaue, H. Rapp, U. Köthe, B. Jähne, and F. A. Hamprecht, *Opt. Eng.* **48**, 013602 (2009).
11. J. P. Godbaz, M. J. Cree, and A. A. Dorrington, *Remote Sens.* **4**, 21–42 (2011).
12. A. P. P. Jongenelen, D. G. Bailey, A. D. Payne, A. A. Dorrington, and D. A. Carnegie, *IEEE T. Instrum. Meas.* **60**, 1861–1868 (2011).
13. A. Dorrington, J. Godbaz, M. Cree, A. Payne, and L. Streeter, *Proc. SPIE* **7864**, 786404 (2011).
14. J. Godbaz, M. Cree, and A. Dorrington, *Proc. SPIE*, **8296**, 829618 (2012).
15. J. P. Godbaz, A. A. Dorrington, and M. J. Cree, 91–116 (Springer, 2013).
16. A. Bhandari, A. Kadambi, R. Whyte, L. Streeter, C. Barsi, A. Dorrington, and R. Raskar, *ACM SIGGRAPH Posters*, 46 (2013).
17. A. Kadambi, R. Whyte, A. Bhandari, L. Streeter, C. Barsi, A. A. Dorrington, and R. Raskar, *ACM T. Graphic.* **32**, 167 (2013).
18. S. K. Nayar, G. Krishnan, M. D. Grossberg, and R. Raskar, *ACM T. Graphic.* **24**, 935–944 (2006).
19. S. Y. Chen, Y. F. Li, and J. W. Zhang, *IEEE T. Image Proc.* **17**, 167–176 (2008).
20. S. Y. Chen (Springer, 2008).
21. S. Fuchs, *Proc. CVPR IEEE*, 3583–3586 (2010).
22. D. Jimenez, D. Pizarro, M. Mazo, and S. Palazuelos, *Proc. CVPR IEEE*, 893–900 (2012).
23. P. Stoica and R. L. Moses (Prentice Hall, 1997).
24. T. Yamaguchi, I. and Zhang, *Opt. Lett.* **22**, 1268–1270 (1997).
25. Y. C. Pati, R. Rezaifar, and P. S. Krishnaprasad, *Signals, Sys., Comp.* **1**, 40–44 (1993).
26. A. Velten, T. Willwacher, O. Gupta, A. Veeraraghavan, M. G. Bawendi, and R. Raskar, *Nat. Commun.* **3**, 745 (2012).
27. J. J. Barton, *Phys. Rev. Lett.* **67**, 3106–3109 (1991).

References

1. D. M. Cash, T. K. Sinha, W. C. Chapman, H. Terawaki, B. M. Dawant, R. L. Galloway, and M. I. Miga, "Incorporation of a laser range scanner into image-guided liver surgery: surface acquisition, registration, and tracking," *Med. Phys.* **30**, 1671–1682 (2003).
2. P. Breuer, C. Eckes, and S. Müller, "Hand gesture recognition with a novel IR time-of-flight range camera—a pilot study," *Computer Vision/Computer Graphics Collaboration Techniques*, 247–260 (Springer, 2007).
3. M. C. Amann, T. Boch, R. Myllyla, M. Rioux, and M. Lescure, "Laser ranging: a critical review of usual techniques for distance measurement," *Opt. Eng.* **40**, 10–19 (2001).
4. Y. Cui, S. Schoun, D. Chan, S. Thrun, and C. Theobalt, "3D shape scanning with a time-of-flight camera," *Proc. CVPR IEEE*, 1173–1180 (2010).
5. J. C. Halimeh and M. Wegener, "Time-of-flight imaging of invisibility cloaks," *Opt. Express* **20**, 63–74 (2012).
6. R. Lange, and P. Seitz, "Solid-state time-of-flight range camera," *IEEE J. Quant. Elect.* **37**, 390–397 (2001).
7. S. Foix, G. Alenya, and C. Torras, "Lock-in time-of-flight (tof) cameras: a survey," *IEEE Sens. J.* **11**, 1917–1926 (2011).
8. A. Kolb, E. Barth, R. Koch, and R. Larsen, "Time-of-Flight sensors in computer graphics," *Proc. Eurographics*, 119–134 (2009).
9. M. Hansard, S. Lee, O. Choi, and R. Horaud, *Time-of-flight cameras: principles, methods and applications* (Springer, 2013).
10. M. Frank, M. Plaue, H. Rapp, U. Köthe, B. Jähne, and F. A. Hamprecht, "Theoretical and experimental error analysis of continuous-wave Time-of-Flight range cameras," *Opt. Eng.* **48**, 013602 (2009).
11. J. P. Godbaz, M. J. Cree, and A. A. Dorrington, "Understanding and ameliorating non-linear phase and amplitude responses in amcw lidar," *Remote Sens.* **4**, 21–42 (2011).
12. A. P. P. Jongenelen, D. G. Bailey, A. D. Payne, A. A. Dorrington, and D. A. Carnegie, "Analysis of errors in tof range imaging with dual-frequency modulation," *IEEE T. Instrum. Meas.* **60**, 1861–1868 (2011).
13. A. Dorrington, J. Godbaz, M. Cree, A. Payne, and L. Streeter, "Separating true range measurements from multi-path and scattering interference in commercial range cameras," *Proc. SPIE* **7864**, 786404 (2011).
14. J. Godbaz, M. Cree, and A. Dorrington, "Closed-form inverses for the mixed pixel/multipath interference problem in amcw lidar," *Proc. SPIE* **8296**, 829618 (2012).
15. J. P. Godbaz, A. A. Dorrington, and M. J. Cree, "Understanding and ameliorating mixed pixels and multipath interference in amcw lidar," *TOF Range-Imaging Cameras*, 91–116, (Springer, 2013).
16. A. Bhandari, A. Kadambi, R. Whyte, L. Streeter, C. Barsi, A. Dorrington, and R. Raskar, "Multifrequency time of flight in the context of transient renderings," *ACM SIGGRAPH Posters*, 46 (2013).
17. A. Kadambi, R. Whyte, A. Bhandari, L. Streeter, C. Barsi, A. A. Dorrington, and R. Raskar, "Coded time of flight cameras: sparse deconvolution to address multipath interference and recover time profiles," *ACM T. Graphic.* **32**, 167 (2013).
18. S. K. Nayar, G. Krishnan, M. D. Grossberg, and R. Raskar, *ACM T. Graphic.* **24**, 935–944 (2006).
19. S. Y. Chen, Y. F. Li, and J. W. Zhang, "Vision processing for realtime 3d data acquisition based on coded structured light," *IEEE Trans. Image Proc.* **17**, 167–176 (2008).
20. S. Y. Chen, *Active Sensor Planning for Multiview Vision Tasks* (Springer, 2008).
21. S. Fuchs, "Multipath interference compensation in time-of-flight camera images," *Proc. CVPR IEEE* 3583–3586 (2010).
22. D. Jimenez, D. Pizarro, M. Mazo, and S. Palazuelos, "Modelling and correction of multipath interference in time of flight cameras," *IProc. CVPR IEEE*, 893–900 (2012).
23. P. Stoica and R. L. Moses, *Introduction to Spectral Analysis* (Prentice Hall, 1997).
24. T. Yamaguchi, I. and Zhang, "Phase shifting digital holography," *Opt. Lett.* **22**, 1268 (1997).
25. Y. C. Pati, R. Rezaifar, and P. S. Krishnaprasad, "Orthogonal matching pursuit: recursive function approximation with applications to wavelet decomposition," *Signals, Sys., Comp.* **1**, 40–44 (1993).
26. A. Velten, T. Willwacher, O. Gupta, A. Veeraraghavan, M. G. Bawendi, and R. Raskar, "Recovering three-dimensional shape around a corner using ultrafast time-of-flight imaging," *Nat. Commun.* **3**, 745 (2012).
27. J. J. Barton, "Removing multiple scattering and twin images from holographic images," *Phys. Rev. Lett.* **67**, 3106–3109 (1991).